

Lysyl Oxidase Inhibition with PAT1251 in 3D Fibroblast Tissue Rings and its Effects on  
Biomechanics

By

Jayla Millender

B.S., University of Connecticut, 2021

B.A., University of Connecticut 2021

Thesis

Submitted in partial fulfillment of the requirements for the Degree of Master of Science  
in the Graduate Program of Biotechnology at Brown University

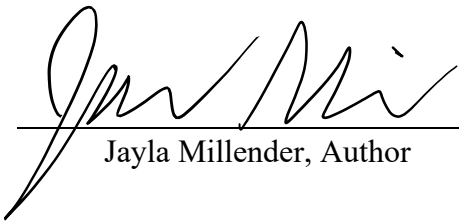
PROVIDENCE, RHODE ISLAND

MAY 2023

AUTHORIZATION TO LEND AND REPRODUCE THE THESIS

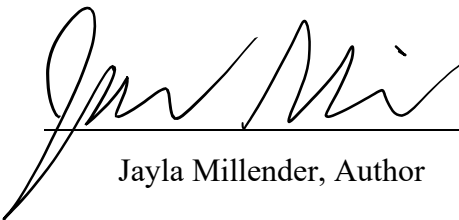
**As the sole author of this thesis, I authorize Brown University to lend it to other institutions for the purpose of scholarly research.**

Date 04/01/2023

  
Jayla Millender, Author

**I further authorize Brown University to reproduce this thesis by photocopying or other means, in total or in part, at the request of other institutions or individuals for the purpose of scholarly research.**

Date 04/01/2023

  
Jayla Millender, Author

This thesis by (Jayla Millender) is accepted in its present form by the Graduate Program in Biotechnology as satisfying the thesis requirements for the degree of Master of Science

Date \_\_\_\_\_ Signature: \_\_\_\_\_  
Dr. Jeffrey Morgan, Advisor

Date \_\_\_\_\_ Signature: \_\_\_\_\_  
Dr. Jacquelyn Schell, Reader

Date \_\_\_\_\_ Signature: \_\_\_\_\_  
Dr. Diane Hoffman-Kim, Reader

Approved by the Graduate Council

Date \_\_\_\_\_ Signature: \_\_\_\_\_  
Dr. Thomas Lewis, Dean of the Graduate School

## Acknowledgements

I would like to express my deepest appreciation to all the people who mentored me and supported me at Brown University. Many thanks to my advisor, Dr. Jeffrey Morgan, for welcoming me to his lab and providing me with personal, professional, and academic support. To Caitlin Hopkins, I am deeply indebted to you for guiding me through multiple challenging protocols and experimental designs. Your valuable feedback was critical in my success. I'd also like to thank Samantha Madnick and Katerina St. Angelo for stepping in and assisting me when personal hardships made completing my thesis project seem impossible. The collaborative and supportive environment created by all members of the Morgan Lab was critical for my success with this project. I also extend my sincere thanks to my readers, Dr. Jacquelyn Schell and Dr. Diane Hoffman-Kim, for taking the time to join my committee and review my work. Lastly, I'd like to thank my friends and family for their love and encouragement throughout my course of study. I would not be here without each and every one of you.

## Table of Contents

<b>Acknowledgements</b> .....	<b>iv</b>
<b>Table of Contents</b> .....	<b>v</b>
<b>Table of Figures</b> .....	<b>vi</b>
<b>Table of Tables</b> .....	<b>vii</b>
<b>Introduction</b> .....	<b>9</b>
Lysyl Oxidase (LOX) Enzyme Superfamily .....	9
Lysyl Oxidase L2 (LOXL2) .....	12
Transforming Growth Factor Beta-1 (TGF- $\beta$ 1) .....	13
TGF- $\beta$ /Smad Pathway .....	13
PAT-1251 as an Inhibitor of LOXL2 .....	14
3D <i>in vitro</i> Human Fibroblast Ring-Shaped Microtissue Model .....	15
Importance of the ECM in Tissue Biomechanics .....	16
<b>Methods</b> .....	<b>19</b>
2D Cell Culturing Conditions .....	19
Fabrication of 3D Ring-Shaped Molds .....	20
Cell Seeding of 3D Ring-Shaped Molds .....	21
TGF- $\beta$ 1 and PAT-1251 Treatment of Microtissues .....	21
Ring Tissue Visualization .....	22
Mechanical Testing of Ring-Shaped Tissues .....	22
Data Analysis .....	23
Statistical Analysis .....	24
<b>Results</b> .....	<b>25</b>
Fibroblasts Self-Aggregate into Ring-Shaped Tissues .....	25
TGF- $\beta$ 1 Increases Cross-Sectional Area and Volume of 3D Ring Tissues .....	26
Treatment of Ring Tissues with PAT-1251 plus TGF- $\beta$ 1 Increases Ring Size .....	27
PAT-1251 Decreases Tissue Biomechanics .....	29
TGF- $\beta$ 1 Increases Tissue Biomechanics .....	29
Treatment with PAT-1251 plus TGF- $\beta$ 1 Decreases Tissue Biomechanics .....	31
PAT-1251 Affects 3D Ring Tissue Morphology .....	31
Ring Morphology Affects CSA and Volume of 3D Ring Tissues .....	35
<b>Discussion and Conclusions</b> .....	<b>38</b>
<b>References</b> .....	<b>42</b>

## Table of Figures

<b>Figure 1.</b> Domain organization of the five members of the lysyl oxidase family .....	10
<b>Figure 2.</b> Enzymatic reaction catalyzed by the lysyl oxidase family of enzymes .....	11
<b>Figure 3.</b> Schematic of TGF- $\beta$ /LOX interaction. ....	14
<b>Figure 4.</b> Structure of PAT-1251 .....	15
<b>Figure 5.</b> Representation of a typical stress-strain curve .....	18
<b>Figure 6.</b> Formation of 3D ring tissue using stainless steel molds with aluminum base.....	25
<b>Figure 7.</b> Conventional view brightfield images of 3D ring tissues .....	26
<b>Figure 8.</b> The cross-sectional area and volume of each ring tissue .....	28
<b>Figure 9.</b> 3D Ring tissues were mechanically tested on day 14 .....	30
<b>Figure 10.</b> 3D tissue ring quality and fitness as a function of treatment .....	34
<b>Figure 11.</b> Average 3D ring tissue $x$ , $y$ thickness as a result of PAT-1251 .....	37

## Table of Tables

<b>Table 1.</b> LOX inhibitor comparison.....	12
---	----

## **Abstract**

Fibrosis occurs when the production of cross-linked collagen fibrils exceeds their degradation [1]. While there are multiple potential triggering stimuli and contributing factors to fibrotic progression, excessive accumulation of ECM components is still the end result. Several tissue types can be affected by fibrosis including skin, liver, heart, lung, intestine, and others. Lysyl oxidases (LOX) and transforming growth factor-beta1 (TGF- $\beta$ 1) contribute to fibrotic progression by increasing total collagen and collagen crosslinking in the ECM [1, 2]. This increased collagen crosslinking increases the elasticity and ultimate tensile strength of the affected tissue [3]. By measuring the tensile properties of TGF- $\beta$ 1 and LOX inhibitor-treated 3D *in vitro* self-assembled tissue ring models, we can show how the biomechanics of these ring tissues can be altered by the addition of different growth factors and drugs.



## Introduction

### Lysyl Oxidase (LOX) Enzyme Superfamily

Extracellular matrix (ECM) synthesis and composition are important in tissue development and biomechanics. Dysregulation of these physiological mechanisms is a key feature of diseases like fibrosis. Fibrosis is a pathological process defined by a surfeit of fibroblast proliferation and excess deposition of extracellular matrix proteins including collagen. Collagen is one of the most abundant proteins in the body. It appears as a fiber-like structure and ultimately plays a large role in the physiological and biomechanical properties of the connective tissues it composes [3, 4]. Under physiological conditions, collagen undergoes three major modifications before reaching its final cross-linked form. In the nuclei of fibroblast cells, there are genes that encode for the biological polymer collagen. These genes are transcribed from DNA to mRNA which is then translated to collagen polypeptides. These polypeptides then travel to the endoplasmic reticulum of the cell where they self-assemble into a more stable structure, trimers. Collagen trimers can then be released from the cell via exocytosis into the ECM. There they self-assemble into collagen fibrils which can then be further stabilized through enzymatic post-translational modifications [4].

A key family of enzymes involved in the post-translational modification of collagen are lysyl oxidases (LOX). The mammalian LOX family is composed of 5 different enzymes: LOX and LOXL 1- 4. The catalytic domain of each lysyl oxidase is the same, but their N-termini differ (**Figure 1**) [5, 6]. LOX binds to its substrate via lysine tyrosylquinone (LTQ) group. The formation and function of this quinone group is dependent on the presence of copper as copper catalyzes the formation of the quinone cofactor [7]. Lysyl oxidase can be inhibited by zinc

through competitive inhibition as zinc will bind to the same binding domain as copper with high affinity. Binding of zinc to the copper-binding region of lysyl oxidases will block LTQ generation – inhibiting LOX activity [8].

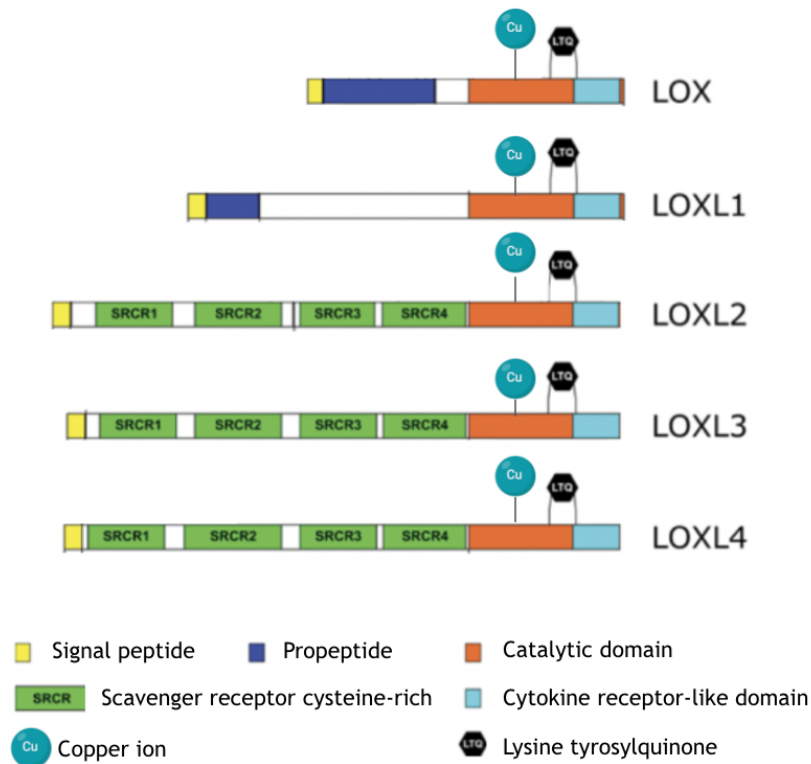


**Figure 1.** Domain organization of the five members of the lysyl oxidase family. Figure adapted from Vallet and Ricard-Blum [6].

Lysyl oxidases act by modifying the amino groups of lysine and hydroxylysine residues in the telopeptide domains of extracellular collagen into aldehyde groups which can interact with adjacent unmodified amino groups (**Figure 2**) [4, 6]. Collagen precursors bind to the LTQ functional group to undergo this transformation. The aldehydes of the collagen precursors then interact with other aldehyde groups or even the unmodified lysine or hydroxylysine residues on other collagen fibrils to form crosslinks [6, 9]. This crosslinking enables collagen to maintain its

biologic activity and increase its stability and tensile strength [4]. Collagen crosslinking contributes to overall ECM stiffness and mechanical properties, namely ultimate tensile strength of collagen fibrils and elasticity of elastic fibers. These crosslinked polymers are relatively resistant to proteases and enzymatic degradation compared to uncrosslinked collagen fibrils [9]. Additionally, LOX protein expression is positively correlated with fibrotic disease in various tissue types [10]. Therefore, preventing collagen crosslinking by inhibiting lysyl oxidase activity may be a suitable target for drug therapies in the treatment of fibrosis.

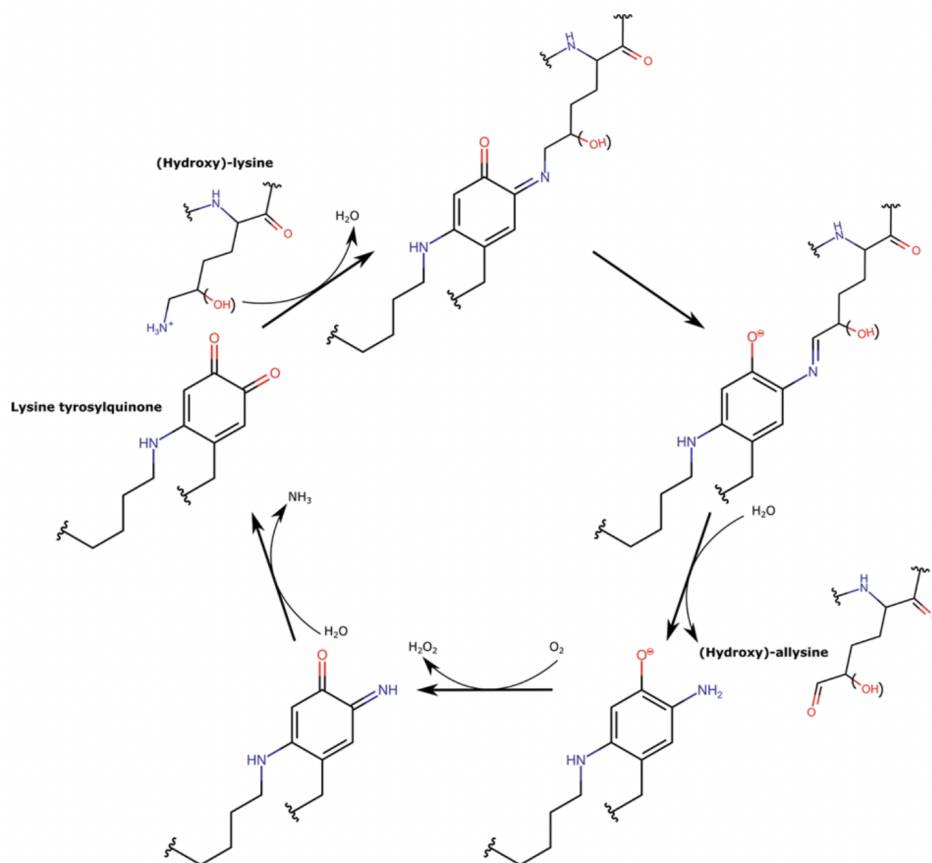


**Figure 2.** Enzymatic reaction catalyzed by the lysyl oxidase family of enzymes. Collagen precursors bind to the LTQ functional group of LOX. LOX then catalyzes the deamination of lysine hydroxylysine residues of collagen precursors. Figure reproduced from Vallet and Ricard-Blum [6].

## Lysyl Oxidase L2 (LOXL2)

Of the lysyl oxidase family, LOX and LOXL2 are the most studied and known to be synthesized by human dermal fibroblasts. Drugs aimed at disrupting collagen crosslinking thus far are focused on the inhibition of these two enzymes, particularly LOXL2 due to the positive correlation between LOXL2 expression and collagen IV quantity [10, 11]. PAT-1251 in particular is of interest to several pharmaceutical companies. Compared to other studied treatments (**Table 1**), PAT-1251 has a unique specificity for LOXL2 and manageable IC<sub>50</sub> of 0.87  $\mu$ M at >400-fold selectivity for the enzyme LOXL2 over LOX [7, 12]. Additionally, previous research suggests LOXL2 may play an important role in the well-known TGF- $\beta$ /Smad pathway-further contributing to collagen crosslinking in the ECM [2, 7].

Characteristic	PAT-1251	PXS 5153A	Heparin	LMW Heparin
MW	399.3Da	475.4Da	~17-20kDa	~3-6.5kDa
Concentration ( $\mu$ g/ $\mu$ l)	$3.4 \times 10^{-4}$	$1.9^{-5}$	0.096	0.4
IC <sub>50</sub> ( $\mu$ M)	0.87	0.040-0.063		
Degree of Inhibition			40%	68%
Specificity	LOXL2	LOXL2/L3		

**Table 1.** LOX inhibitor comparison. Table comparison of molecular weight, drug concentration, IC<sub>50</sub>, degree of inhibition and specificity of PAT-1251, PXS5153A, Heparin and low molecular weight (LMW) heparin as potential therapeutic agents targeting collagen [7, 9, 12-15].

## **Transforming Growth Factor Beta-1 (TGF- $\beta$ 1)**

TGF- $\beta$  is a cytokine growth factor that exists in three isoforms. Each isoform is synthesized in fibroblast cells and released into the ECM in a latent state as part of a latent complex composed of a TGF- $\beta$  isoform and its respective latent TGF- $\beta$  binding protein (LTBP). LTBP facilitates the secretion of TGF- $\beta$ 1 from the fibroblast in its inactive form and directs its release from the latent complex and into its active form [16, 17]. TGF- $\beta$ 1 specifically is central in the development of fibrosis. TGF- $\beta$ 1 is a key activator of fibroblasts and the pathogenesis of fibrosis [18, 19].

### **TGF- $\beta$ /Smad Pathway**

TGF- $\beta$ 1 ligands bind to the TGF- $\beta$  I-II receptor heteromeric transmembrane complex. This activates the intracellular Smad2/Smad3 complex via phosphorylation. The phosphorylated Smad2/Smad3 complex then binds to Smad4 to translocate to the nucleus. In the nucleus, the Smad2/3/4 complex will either bind by itself or with AP-1 to the promoter regions of the LOX family genes to increase their transcription [2]. TGF- $\beta$  I-II receptor activation also activates JNK via phosphorylation. Phosphorylated JNK can then translocate to the nucleus where it will similarly either bind directly to the promoter regions of the LOX genes or with AP-1 to the promoter regions of the LOX genes to regulate their transcription and ultimately their expression. The translated LOX proteins will then cross the cellular membrane and exit the cell into the ECM where they will participate in collagen and elastin crosslinking (**Figure 3**) [2, 5].

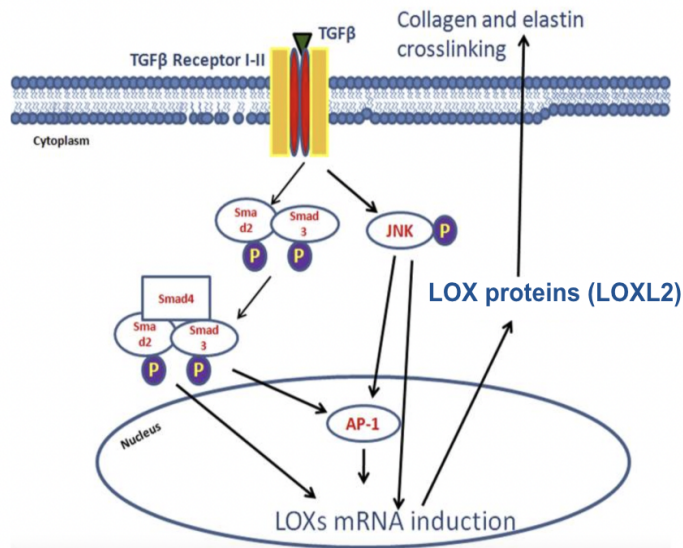


**Figure 3.** Schematic of TGF- $\beta$ /LOX interaction. Proposed mechanism of TGF- $\beta$  regulation of LOX in human fibroblasts and implications on fibrosis. Figure adapted from Sethi et al [2].

### PAT-1251 as an Inhibitor of LOXL2

PAT-1251 is an irreversible, small molecule inhibitor of LOXL2 that works to inhibit collagen crosslinking in the ECM [7, 20]. PAT-1251 has a benzylamine base with 2-substituted pyridine-4-methanamines (**Figure 4**) [7]. The LOXL2 inhibitor's proposed mechanism of action is that it irreversibly binds to LOXL2 at its quinone functional group, LTQ, preventing it from interacting with collagen fibrils in the ECM. As a result, these fibrils will be unable to undergo the necessary post-translational processing to enhance tissue stiffness, ultimate tensile strength and other critical biomechanical properties heightened in fibrotic progression [21]. The study of LOX inhibitors as a potential drug therapy in the treatment of fibrotic diseases is a relatively new

field and additional research is needed to provide a full profile of each potential treatment.

Despite this, PAT-1251 is the first of its class to move onto Phase 2 clinical trials [20, 22, 23].

PAT-1251 is the first irreversible binding inhibitor of LOXL2 to advance to clinical trials [23]. After successful completion of phase 1 study in healthy patients, PAT-1251 was determined to be well-tolerated and safe for oral administration [7, 20, 22, 23]. Phase 2 trials began in 2018 for the use of PAT-1251 in treating patients with myelofibrosis and other conditions [20].

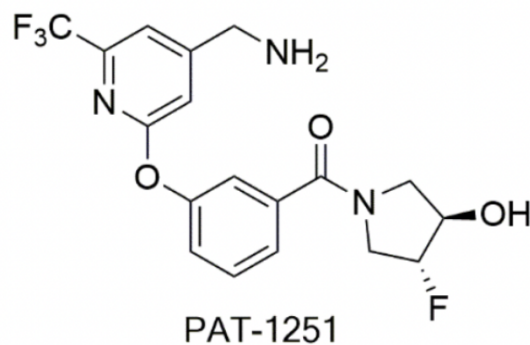


**Figure 4.** Structure of PAT-1251 Figure adapted from Ferreira et al [7].

### **3D *in vitro* Human Fibroblast Ring-Shaped Microtissue Model**

A 3D *in vitro* model was developed by the Morgan Lab at Brown University that allows cell-mediated self-assembly of ring-shaped tissues in a non-adherent environment [24]. This 3D cell-culturing model produces cell-dense tissues that synthesize a collagen-rich ECM environment that is highly aligned and closely mirrors the observed mechanical and histological properties of native connective tissues [24]. One of the key advantages of this model is its elimination of exogenous polymers and scaffolding materials. Existing *in vitro* models are

predominantly reliant on cell-seeded scaffolds that promote crosstalk between the seeded cells and the scaffold structure [24-26]. This interaction can alter overall cell dispersion, ECM synthesis and composition, collagen alignment and ultimately tissue biomechanics [24, 25]. Using the Morgan fibrotic system, human dermal fibroblasts are seeded in a non-adherent ring-shaped agarose mold. This allows the cells to be guided to the bottom of the mold by gravity and self-assemble around a central agarose peg. By culturing fibroblasts in this model, the cells will eventually form a microtissue ring that can be removed from the peg and used for biomechanical testing [24]. Utilizing this model, Wilks *et. al.* optimized the cell seeding density, mold formation and mechanical testing environment for future experimentation.

### **Importance of the ECM in Tissue Biomechanics**

In the ECM of human fibroblasts, collagen-based structures compose a large portion of the total ECM. Collagen based structures such as tendons and other ligamentous structures account for approximately 80% of the total ECM while the fibroblasts or other cells growing around the ECM account for the remaining 20% [26, 27]. The large volume of collagen fibers compose complex, multilayered structures of crosslinked collagen fibrils that contribute to the overall tissues.

Hooke's Law and Young's modulus are heavily relied on in analyzing the mechanical properties of ring tissues. Hooke's Law is a fundamental law in physics that describes the direct proportionality between the force applied to an object and the induced strain [27]. Young's Modulus (or Elastic Modulus) is a constant coefficient of stiffness-indicating how easily an object can be stretched or deformed [27, 28]. In biomechanical testing and analysis, Young's



Modulus for a given object can be calculated using stress/strain data or a stress-strain curve (**Figure 5**) [27]. The terms “stress” and “strain” are used to describe externally applied forces to an object and that object’s ability to resist those forces. When an external force is applied to a tissue, the inner structure of the tissue, the cellular matrix, will undergo physical changes to resist the external force [27]. The internal force created inside the tissue on which the external force is applied is referred to as “stress.” Stress is measured in units of megapascals (MPa) and is calculated by dividing the external force by the area to which it is applied [27]. The total deformation to the tissue as a result of the externally applied force is referred to as “strain.” Stress and strain can be graphed together to create a stress-strain curve (**Figure 5**) [27].

Materials that are considered brittle have stress-strain curves that are more linear in shape with the yield point, UTS, and point of fracture all being the same. Materials that exhibit more plastic behavior will have stress-strain curves with a small MTM as very little stress is required to produce deformation; however, these materials do not often have a true failure or “breaking point” due to their high plasticity and malleability [27]. Ductile materials have stress-strain curves that appear just between those of brittle and plastic materials. Ductile materials have a larger MTM than plastic materials but less than brittle ones however they do exhibit a period of plasticity unlike their brittle counterparts [27]. The stress strain curve of the cultured ring-shaped tissues is expected to have a large MTM and UTS; however, these are expected to change after different drug treatments [24].

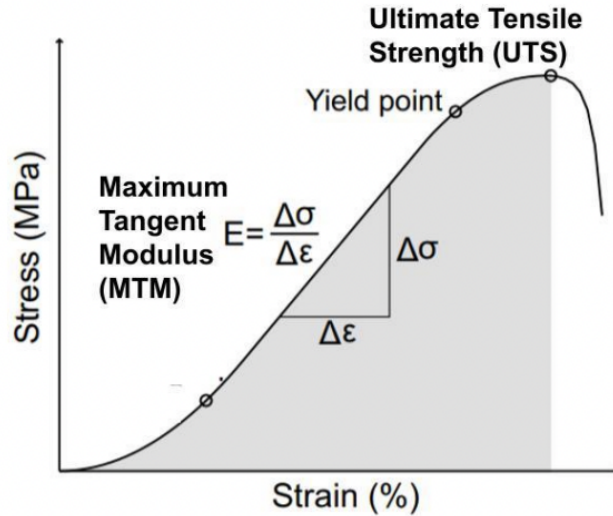


**Figure 5.** Representation of a typical stress-strain curve. Strain is measured as a percentage of change in length. Stress is measured in the unit MPa. Increasing stress applied to an object is positively correlated with strain percentage as the object undergoes incremental deformation. The linear portion of the curve, before the ultimate tensile strength (UTS) point, represents the maximum tangent modulus (MTM) of the object or material. The maxima of the curve is marked by the point labeled UTS. This point represents the total amount of stress in units of MPa that were applied to the tested specimen before it is permanently deformed or broken as with ring-shaped tissues. The yield point marks the total stress that can be applied to the specimen before it no longer exhibits elastic behavior, or the ability to return to its original form. Figure adapted from Ristaniemi et. al. [27].

This research is focused on quantitatively analyzing the effect of PAT-1251 and TGF- $\beta$ 1 treatment on the biomechanical properties of 3D microtissues formed using this *in vitro* model design. The drug treatment groups being studied are control, PAT-1251 (10 $\mu$ M) treated tissues, TGF- $\beta$ 1 (10 ng/mL) treated tissues and tissues treated with both PAT-1251 and TGF- $\beta$ 1 at those respective concentrations. Top brightfield images of these treatment groups are obtained on days 1, 7 and 14. On day 14, the biomechanics of randomly selected tissues from each group are measured to determine the effect of each drug treatment on tissue ring mechanical properties.

## Methods

### 2D Cell Culturing Conditions

Cells used for these experiments were juvenile normal human dermal fibroblasts (JNHDF) purchased from PromoCell, Heidelberg, Germany. Cells were previously cultured, passaged and spun down for storage in a liquid nitrogen cryotank. For the purpose of these experiments, cells at passage 4 (P4) were thawed from the cryotank and cultured in pre-made cell culture medium. This culture medium contained high glucose, L-glutamine, phenol red, and sodium pyruvate DMEM (Dulbecco's Modified Eagle's Medium) (#11995073, Thermo Fisher Scientific, Grand Island, NY). Culture medium also contained 10% fetal bovine serum (FBS) (#100-500, Gemini Bio, Sacramento, CA) and 1% penicillin/streptomycin (#091670249, Thomas Scientific, Swedesboro, NJ) to produce complete media (CM). Cells were cultured in T-175 flasks in an incubator set at 37°C and 10% CO<sub>2</sub>. When cells reached 80-90% confluency, they were passaged into new flasks. For passaging, cell culture medium was carefully aspirated out of the flask. Cells were then washed with 30 mL phosphate-buffered saline (PBS) (#MT21040CM, Fisher Scientific, Manassas, VA). PBS was then carefully aspirated out of the flask and replaced with 0.05% trypsin (#SH3004201, Thermo Fisher Scientific) in PBS and incubated for 5 minutes. Cells were visualized under a Nikon Eclipse TS100 microscope (Nikon, Tokyo, Japan) at 4x magnification to confirm cell dislodgement from the flask surface. Following this, 20 mL of CM was added to stop trypsinization. This solution was then pipetted into 50 mL conical tubes and centrifuged at 800 rpm for 5 minutes. Tubes were then examined to confirm formation of cellular pellets. Remaining medium was carefully aspirated out of the conical tube to ensure no disturbance of the pellet. Cells were resuspended in 5 mL CM from which 10 µL was micropipetted into hemocytometer for cell counting. Finally, cells were plated in new T-175

flasks at a density of approximately  $5.0 \times 10^3$  cells/flask. CM was refreshed 3x/week. Cells were regularly passaged from P4 to P8.

### **Fabrication of 3D Ring-Shaped Molds**

Ring-shaped molds were made following an established protocol by the Morgan Laboratory. Benjamin T. Wilks designed the gel molding-system using CAD software (SolidWorks Corporation, Concord, MA). The molding system consists of two major components: 24 stainless steel inserts and one aluminum holder. The aluminum holder contained 24 holes, one for each stainless steel insert. The holder was designed to sit over the top of an open 24-well plate, with each insert aligned for each well. Into each well of the 24-well plate, 1.5 mL of 2% molten agarose (w/v) (#BP160-500, Fisher Scientific, Hampton, NH) in PBS was pipetted into each well. The aluminum holder with all 24 stainless steel inserts was then placed on top of the plate. The agarose was allowed to cool for 15 minutes before each of the inserts was removed from their respective well, careful to not disturb the ring-shaped mold and central peg formed by the mold. After removal of each insert and the aluminum holder, each well contained a molded agarose gel with a 5 mm diameter central peg and a surrounding circular trough 0.75 mm wide. Each agarose gel was equilibrated with 1mL pre-made serum-free media (SFM) composed of high glucose, L-glutamine, phenol red, and sodium pyruvate DMEM and 1% penicillin/streptomycin. Gels were then incubated at 37°C and 10% CO<sub>2</sub>. Three medium changes were performed with at least 1 hour between changes before gels were used for cell seeding.

### **Cell Seeding of 3D Ring-Shaped Molds**

Cells were seeded into 3D ring molds at P6-P8. Cells were passaged as described above. After cell counting using the hemocytometer, enough cell-suspended media was pipetted from the 50mL conical tube to a new tube to seed the desired number of ring-shaped molds (50) at a density of 300,000 cells/ring. This conical tube was then centrifuged at 800 rpm for 5 minutes. Tubes were then re-examined to confirm formation of the cellular pellet. Remaining medium was carefully aspirated out of the conical tube. Cells were resuspended in 3.75 mL of pre-made 50:50 media as previously described [29]. This 50:50 media was composed of equal parts serum free plus (SFM+) and serum free media advanced (SFMA). The SFM+ contained high glucose, L-glutamine, phenol red, and sodium pyruvate DMEM (#11995073, Thermo Fisher Scientific, Grand Island, NY) supplemented with 50 ug/mL L-proline (#BP392-100, Fisher Scientific) and 0.1mM 2-phospho-L-ascorbic acid trisodium salt (#49752, Sigma-Aldrich) and 1% penicillin/streptomycin (#091670249, Thomas Scientific, Swedesboro, NJ). The SFMA contained advanced DMEM (#12491015, Thermo Fisher Scientific) supplemented with 4mM Glutamax (#35-050-061, Fisher Scientific) and 1% penicillin/streptomycin (#091670249, Thomas Scientific, Swedesboro, NJ). From this resuspended solution, 0.75  $\mu$ l was then added to the trough of each gel. Cells were allowed to settle for 1 hour before 1 mL of 50:50 media was added to each gel. Gels were then incubated at 37°C and 10% CO<sub>2</sub> for 24 hours.

### **TGF- $\beta$ 1 and PAT-1251 Treatment of Microtissues**

Approximately 24 hours after initial cell seeding, media for each gel was changed and rings were treated with PAT-1251, TGF- $\beta$ 1, PAT-1251 plus TGF- $\beta$ 1 or left as an untreated control. TGF- $\beta$ 1 (#100-21, Peprotech) and PAT-1251 (#HY-107422, MedChemExpress) were

reconstituted and aliquoted according to manufacturer's protocol. Each well of the 24-well plate contained 1.5 mL of agarose gel equilibrated with 1 mL of removable 50:50 culture media. Pre-aliquoted TGF- $\beta$ 1 and PAT-1251 were added to 50:50 media to achieve final concentrations of 10 ng/mL and 10  $\mu$ M respectively after equilibration with the agarose gel. Culture media for all treatment groups was refreshed 3x/week with growth factor and drug.

### **Ring Tissue Visualization**

Conventional ( $x, y$ ) imaging was performed on each gel on days 1, 7 and 14. Brightfield images of the gels were taken on a Nikon Eclipse Ts2 microscope (Nikon, Tokyo, Japan) at 2x magnification. Images of the top and bottom halves of each gel were obtained and later pairwise stitched together using ImageJ. After conventional imaging of each gel was performed on day 14, gels were removed from their respective wells using a spatula and placed in individual 60mL dishes. In the dish, one side of the circular gel was removed using a razor blade, careful to not disturb the ring tissue around the central peg. Cut gels were then placed in 8-well square plates (#167064, Thermo Fisher Scientific) with the cut side facing the bottom of the well for side-view ( $z$ ) imaging at 2x magnification.

### **Mechanical Testing of Ring-Shaped Tissues**

Mechanical testing of ring tissues was performed on an Instron tensile tester (35943, Norwood, MA) using a 5N load cell with 5mN resolution. Mechanical testing was performed on day 14 of 3D-cell culturing after conventional and side-view imaging was completed. Rings were dissected from their agarose molds and placed over two custom 3D-printed grippers made from glass-filled nylon (#PA614-GS, ProtoLabs). Grippers were placed together for a total diameter of

3mm. Once the grippers were loaded onto the Instron, the gap between grippers was extended to 2mm to reach a total diameter of 5mm. Test protocols were run as previously described [29] such that the two grippers moved away from each other at a rate of 0.1% initial length/second, displacing the ring. Load (N) and extension (mm) were sampled at 20 Hz. Tests were terminated at tissue failure. Broken rings were snap frozen in liquid nitrogen and stored at -80°C.

## Data Analysis

Mechanical data analysis was performed using an established protocol [24]. The mechanical testing protocol was adapted from Adebayo, *et al.* and Gwyther, *et al.* [30, 31]. The method for data analysis was adapted from Ristaniemi *et al.* [27]. The biomechanical properties for each tensile tested tissue were determined using the ultimate tensile strength (UTS), maximum tangent modulus (MTM), and failure strain. These values were obtained using a custom Python 3.6 (Python Software Foundation) code run on Jupyter Notebook [24]. Raw load measurements were normalized in this process to eliminate drag force generated by the grippers when no sample tissue was loaded. All calculated engineering UTS and MTM values were then normalized to the CSA of each ring. Engineering stress and strain values are only valid for small deformations which are not applicable to many biological samples including fibroblast ring tissues [29]. True stress and strain values were also calculated assuming overall tissue volume conservation and uniform tissue deformation during tensile testing.

For assessing ring tissue quality and fitness for mechanical testing, conventional view brightfield images were uploaded through custom Python 3.6 code produced by Yanying Wu, M.S, and run on Jupyter Notebook. Images were either accepted or rejected by the code based on the programs ability to detect a circular ring tissue around a central agarose peg. Images were

rejected if no uniform ring was detected, rings were too thin or asymmetric, or for poor image quality. Accepted and rejected images were verified manually. Accepted images were assigned a fitness value by the software. Fitness value  $<10,000$  is acceptable with a perfect fit = 0. Values  $>10,000$  indicate questionable ring symmetry.

### **Statistical Analysis**

All data were graphically and statistically analyzed using Prism 9.0 (GraphPad Software, Sand Diego, CA). Each point on a graph represents a separate ring tissue. Vertical lines represent the mean  $\pm$  standard deviation. Natural variance between groups was calculated using ordinary one-way ANOVA with Turkey's multiple comparisons test and one sample t and Wilcoxon test. For each scatter plot and bar graph, the unique \* represents statistical significance ( $p<0.05$ ) between experimental groups, \*\* denotes  $p<0.005$ , and \*\*\* denotes  $p<0.001$  and \*\*\*\* denotes  $p<0.0001$ .



## Results

### Fibroblasts Self-Aggregate into Ring-Shaped Tissues

To produce the 3D ring tissues, human fibroblasts were seeded into the circular troughs of molded agarose gels as depicted in **Figure 6**. Due to the non-adherent surface of the agarose molds, the cells settled to the bottom of the troughs where they self-aggregated into ring-shaped tissues within 24 hours. Brightfield microscopic images taken 24 hours after initial cell seeding confirmed this process (**Figure 7**). After day 1 brightfield imaging, rings were then treated with either 10  $\mu$ M PAT-1251, 10 ng/mL TGF- $\beta$ 1 or TGF- $\beta$ 1 plus PAT-1251. Untreated rings served as a control. Rings were regularly treated with their respective drug and/or growth factor over the course of 14 days.

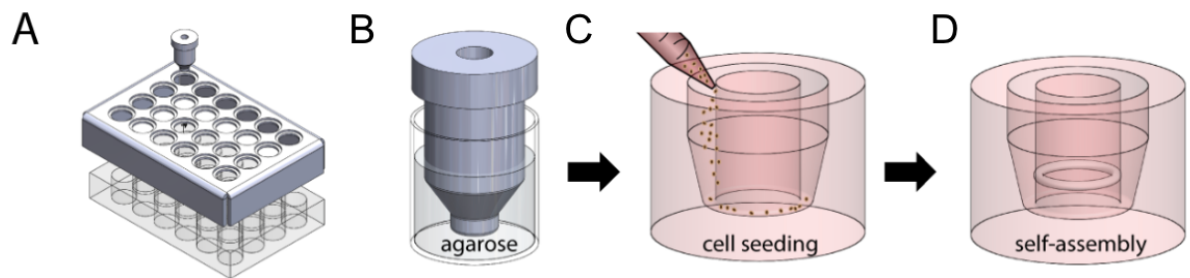


**Figure 6.** Formation of 3D ring tissue using stainless steel molds with aluminum base. (A) Schematic figure of the two-part metal mold. (B) Stainless steel inserts were embedded into wells containing 2% liquid agarose to produce troughs for cell seeding with a 5mm central peg. (C) Each molded well was seeded with  $3 \times 10^5$  fibroblasts which self-assembled to a 3D ring-shaped tissue within 24 hrs. (D). Figure adapted from Wilks et. al. [29].

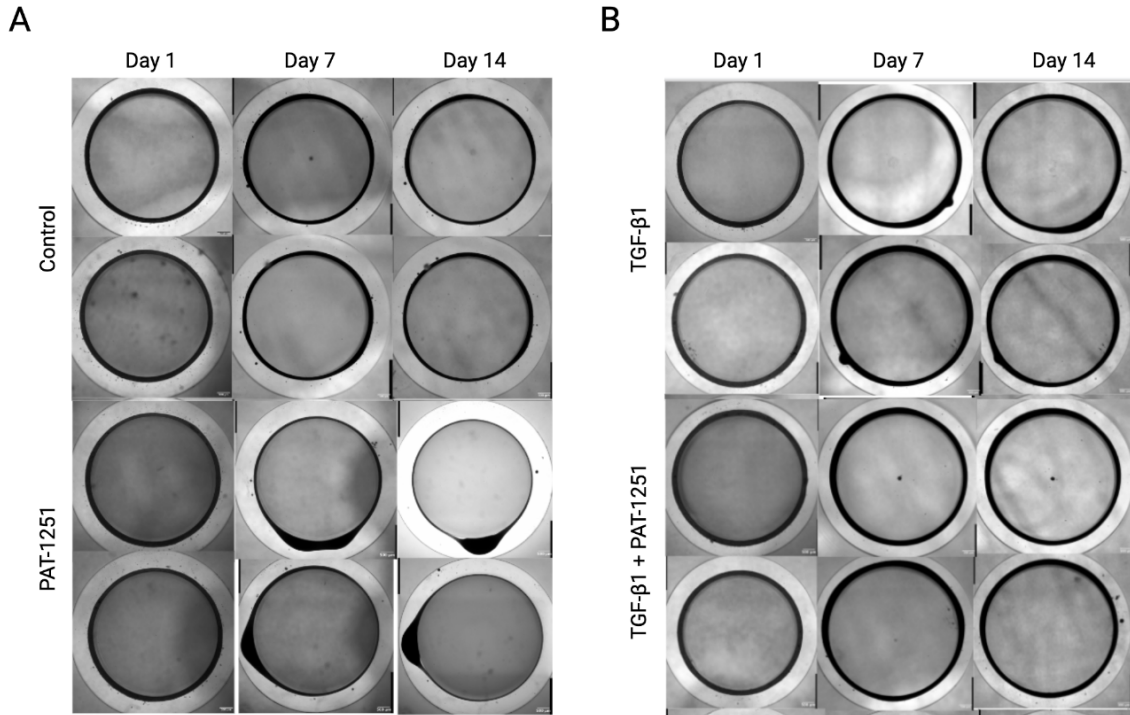


**Figure 7.** Conventional view brightfield images of 3D ring tissues. Brightfield imaging was performed 24 hrs. after cell seeding (day 1) and on days 7 and 14. A slight decrease in ring thickness was observed in the control rings (A) and an even more notable decrease in ring thickness was observed in rings treated with PAT-1251. An increase in ring thickness was observed in the TGF- $\beta$ 1 and TGF- $\beta$ 1 plus PAT-1251 groups (B).

### TGF- $\beta$ 1 Increases Cross-Sectional Area and Volume of 3D Ring Tissues

On day 14, conventional and side-view brightfield images were taken of each ring prior to tensile testing. Several measurements of ring thickness were taken from both views (**Figure 8B-C**). The cross-sectional area (CSA) and volume of rings treated with PAT-1251, TGF- $\beta$ 1 and TGF- $\beta$ 1 plus PAT-1251 were calculated using ring thickness measurements from conventional ( $x, y$ ) and side view ( $z$ ) brightfield images (**Figure 8A**). CSA and volume metrics were then compared between experimental groups and to control (**Figure 8D-E**). At this time point, rings

treated with TGF- $\beta$ 1 alone were noted to be significantly larger in size compared to control, analogous to previously published values [24]. Similarly, TGF- $\beta$ 1 treated rings displayed significantly larger CSA and volume values compared to rings treated with PAT-1251. Despite distinct morphological changes observed in tissues treated with PAT-1251, no difference in CSA or volume was noted between PAT-1251 and control. However, a distinct difference in CSA and volume was noted between PAT-1251 vs TGF- $\beta$ 1 plus PAT-1251 ( $p < 0.001$ ).

### **Treatment of Ring Tissues with PAT-1251 plus TGF- $\beta$ 1 Increases Ring Size**

Interestingly, rings treated with TGF- $\beta$ 1 plus PAT-1251 did not exhibit CSA and volume values similar to those of the control group, contrary to the initial hypothesis that ring size would be unaffected by treatment of TGF- $\beta$ 1 plus PAT-1251 due to potential negating effects.

Interestingly, rings treated with TGF- $\beta$ 1 plus PAT-1251 were comparable in size to ring tissues treated with TGF- $\beta$ 1 alone. Mean CSA of TGF- $\beta$ 1 and combination treated rings were  $7.4 \times 10^4 \mu\text{m}^2$  and  $7.9 \times 10^4 \mu\text{m}^2$  respectively and mean volume for the two groups were approximately  $1.2 \times 10^9$  and  $1.3 \times 10^9 \mu\text{m}^3$  respectively. No significant variance in size was observed between rings treated with TGF- $\beta$ 1 plus PAT-1251 and those treated with TGF- $\beta$ 1 ( $p > 0.05$ ) (**Figure 8D-E**).

However, a significant difference in ring CSA and volume was observed between control and combination treatment groups ( $p < 0.0001$ ). An over 2-fold increase in CSA was overserved from control ( $3.6 \times 10^4 \pm 6.6 \times 10^3 \mu\text{m}^2$ ) to combination ( $7.9 \times 10^4 \pm 9.8 \times 10^3 \mu\text{m}^2$ ) treated rings. The same increase was seen in tissue volume as well with control ( $5.9 \times 10^8 \pm 1.0 \times 10^8 \mu\text{m}^3$ ) and combination ( $1.3 \times 10^9 \pm 1.6 \times 10^8 \mu\text{m}^3$ ) experimental groups.

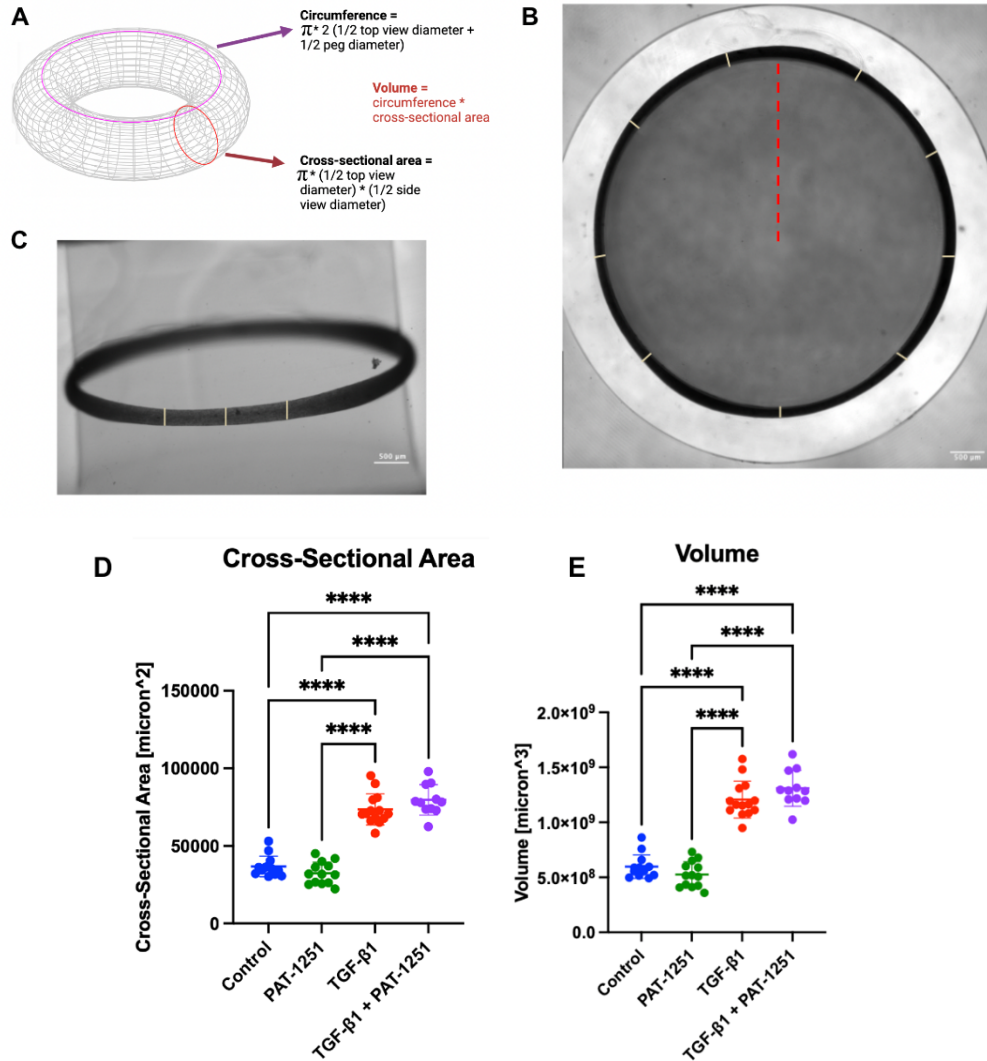


**Figure 8.** The cross-sectional area and volume of each ring tissue were calculated using x, y, z measurements from conventional and side-view brightfield images. (A) Labeled schematic of ring tissue highlighting circumference (purple) and cross-sectional area (red) with their respective formulas. Both formulas require ring thickness to be measured along the x, y and z dimensions through conventional and sideview brightfield imaging. (B) Conventional view brightfield image of a control ring tissue at day 14. Yellow lines represent tissue thickness measurements. Red dashed line represents peg radius of 2500  $\mu\text{m}$ . White scale bar 500  $\mu\text{m}$ . (C) Side view brightfield image of same control tissue at day 14. Yellow lines represent thickness measurements. White scale bar 500  $\mu\text{m}$ . (D) Calculated ring tissue cross-sectional areas as a result of different treatment. (E) Calculated ring tissue volumes as a result of different treatment. For both graphs, n=12, 12, 11 and 11 for control, PAT-1251, TGF- $\beta$ 1 and TGF- $\beta$ 1 plus PAT-1251 rings respectively. \*\*\*\* denotes  $p < 0.001$ .

### **PAT-1251 Decreases Tissue Biomechanics**

To determine if tissue biomechanics were altered by PAT-1251 treatment, rings from each experimental group were subjected to tensile testing on day 14. Ring tissues were placed over 3D-printed grippers and extended to a starting diameter of 5mm (**Figure 9A-B**). Stress-strain curves obtained from mechanical testing were then used to calculate the ultimate tensile strength (UTS) and maximum tangent modulus (MTM) to measure tissue strength and stiffness respectively. All values were normalized to the CSA of each ring.

Compared to control, PAT-1251 significantly reduced tissue strength and stiffness. An over 3-fold decrease in engineering and true UTS was observed ( $p < 0.0001$  and  $p < 0.0005$  respectively) after treatment with PAT-1251 alone. Similarly, a 3-fold decrease in both engineering and true MTM was observed ( $p \leq 0.0001$  for both).

### **TGF- $\beta$ 1 Increases Tissue Biomechanics**

Additional rings were treated with 10 ng/mL TGF- $\beta$ 1 alone as it thought to be a key driver of fibrosis [16, 17, 19]. Previous studies using this 3D fibroblast ring tissue model have shown an increase in tissue size and biomechanics after treatment with TGF- $\beta$ 1 [24]. TGF- $\beta$ 1 was included in this study to show this same increase and to then see if PAT-1251 exhibits the same effects it does alone if it is added to a TGF- $\beta$ 1 stimulated environment. Rings treated with TGF- $\beta$ 1 alone showed a significant increase in tissue strength and stiffness compared to control ( $p < 0.05$ ). These results are consistent between the engineering and true UTS and MTM values (**Figure 9C-F**).

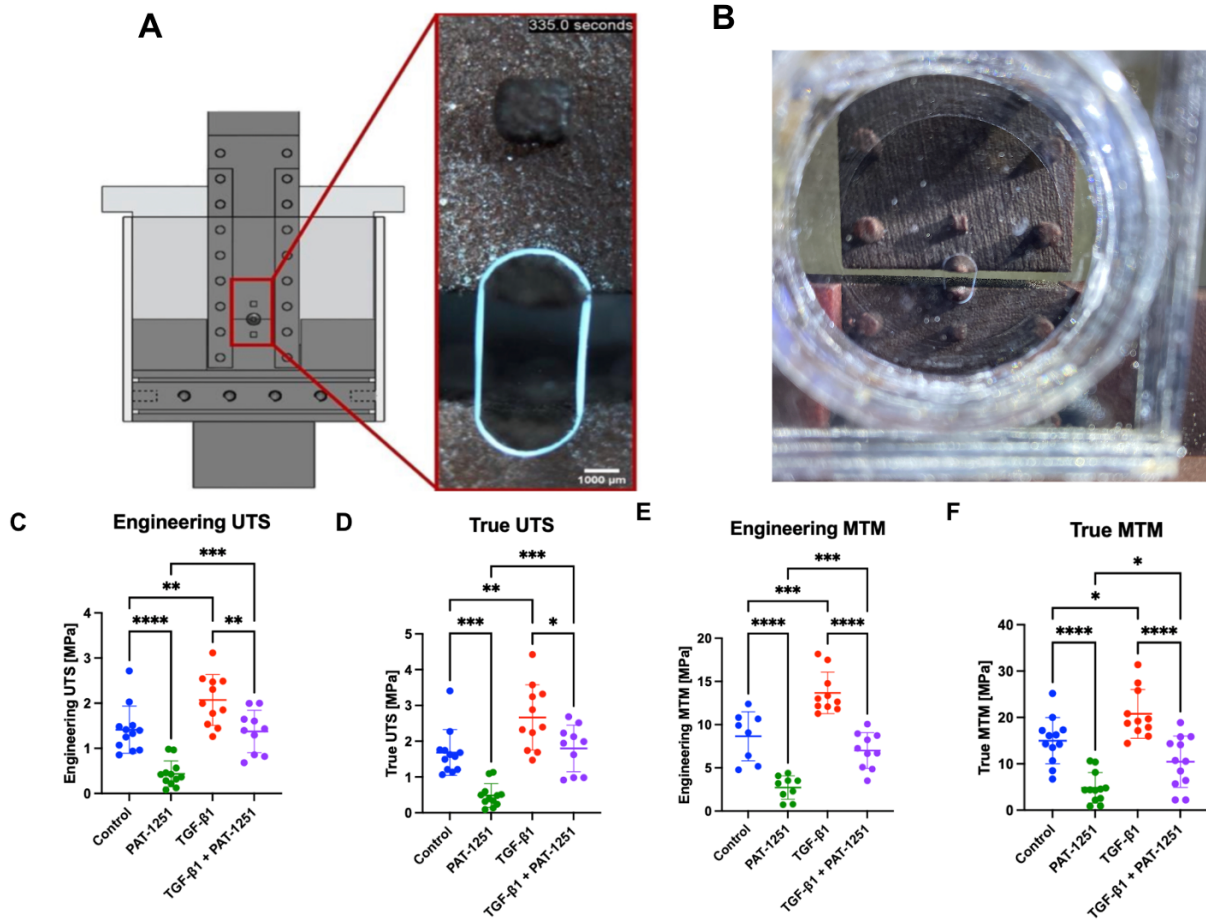


**Figure 9.** 3D Ring tissues were mechanically tested on day 14. (A, B) Ring tissues were placed over 3D-printed grippers and the gap between them was extended. Figure adapted from Wilks et al. [24]. Tissue strength (C, D) and stiffness (E, F) was quantified using the cross-sectional area of each ring and either engineering (C, E) or true stress and strain values (D, F). Compared to control, tissue strength increased with treatment of TGF- $\beta$ 1 alone (C, D). However, tissue strength and stiffness decreased after treatment with PAT-1251 alone. A decrease in biomechanics was seen with TGF- $\beta$ 1 plus PAT-1251 compared to TGF- $\beta$ 1 alone. No significant difference in tissue strength or stiffness was observed between ring tissues treated with TGF- $\beta$ 1 plus PAT-1251 and control. For all graphs, the unique character \* denotes  $p < 0.05$ , \*\* denotes  $p < 0.01$ , \*\*\* denotes  $p < 0.0005$  and \*\*\*\* denotes  $p < 0.0001$ .

## **Treatment with PAT-1251 plus TGF- $\beta$ 1 Decreases Tissue Biomechanics**

As previously mentioned, treatment with TGF- $\beta$ 1 alone produced stiffer and stronger rings compared to control. Despite their comparable size to TGF- $\beta$ 1 rings, tissues treated with TGF- $\beta$ 1 plus PAT-1251 exhibited significantly decreased biomechanics. Mean engineering and true UTS values of combination treated rings were approximately 1.4 and 1.800 MPa respectively ( $p < 0.01$  and  $p < 0.05$  compared to TGF- $\beta$ 1 alone) (**Figure 9C-D**). Similar variance was observed with the mean engineering and true MTM values of combination treated rings 7.003 MPa and 10.44 MPa respectively ( $p < 0.0001$  for both) (**Figure 9E-F**). No difference in biomechanics was observed between control and TGF- $\beta$ 1 plus PAT-1251 samples ( $p > 0.05$ ).

Combination treated rings did however appear stronger than rings treated with PAT-1251 alone ( $p < 0.005$  for engineering and true UTS values). Mean tissue stiffness however was not consistently different between these two experimental groups. The engineering MTM for samples treated with TGF- $\beta$ 1 plus PAT-1251 (7.0 MPa) was approximately 2.5x greater than that of samples treated with PAT-1251 alone (2.7 MPa) ( $p < 0.005$ ) (**Figure 9E**). No significant difference however was found when true MTM values were calculated assuming overall tissue volume conservation and uniform tissue deformation ( $p > 0.05$ ) (**Figure 9F**). This inconsistency suggests a potentially more complex relationship between TGF- $\beta$ 1 and LOX signaling affecting biomechanics than what is currently known.

## **PAT-1251 Affects 3D Ring Tissue Morphology**

When  $x$ ,  $y$  and  $z$  dimension ring thickness measurements were taken, they were taken from nine, equidistant yet random locations across the ring tissue. Following this protocol, no

significant difference in ring CSA or volume was observed after treatment with PAT-1251 alone ( $p>0.05$ ). Despite this finding, ring abnormalities were observed in brightfield images of rings after 14 days of treatment with PAT-1251. PAT-1251 rings appeared asymmetric compared to other experimental groups and control (**Figure 7**).

To further investigate the effects of PAT-1251 on the morphology of 3D ring tissues, rings were treated with 10  $\mu\text{M}$  of PAT-1251 at initial cell seeding (day 0). Conventional view brightfield imaging was then performed 24, 48 and 72 hrs. after initial treatment (**Figure 10A-B**). No media exchange occurred during this time frame. Collected images were then run through a custom Python code to determine their overall Quality and Fitness. Images were first either accepted or rejected (**Figure 10C**) by the program. Quality was determined by the number of images from each treatment group that were accepted. These accepted images were then assigned a fitness value  $\geq 0$  (**Figure 10D**).

A significant drop in ring quality was observed 48 and 72 hrs. after seeding with PAT-1251 treatment. After 24 hrs. in treatment, all 22 control rings remained intact while only 16 of the 22 PAT-1251 rings were intact. Over the next 2 days, only 1 control ring would be rejected by the Python program for ring breakage while the number of rejected PAT-1251 rings increased to 14 after 48 hrs. and to 15 after 72 hrs. Interestingly, more PAT-1251 rings broke over the continuous 72 hr. period compared to control ( $p<0.01$ ).

All accepted images from the Python program were assigned a unitless fitness value in accordance with its overall asymmetry. Generally, fitness values  $<10,000$  are deemed suitable for tensile testing while values  $>10,000$  are not. A fitness value equal to 0 represents a ring tissue with perfect symmetry. Calculated from brightfield images taken 72 hrs. after initial cell seeding and drug treatment, fitness values from both control and PAT-1251 rings are shown in



**Figure 10D.** A significant difference in average ring fitness between groups is seen ( $p < 0.05$ ) with the mean fitness value for control being 3,062 and the same value for PAT-1251 rings being 5,805 - both values are unitless.

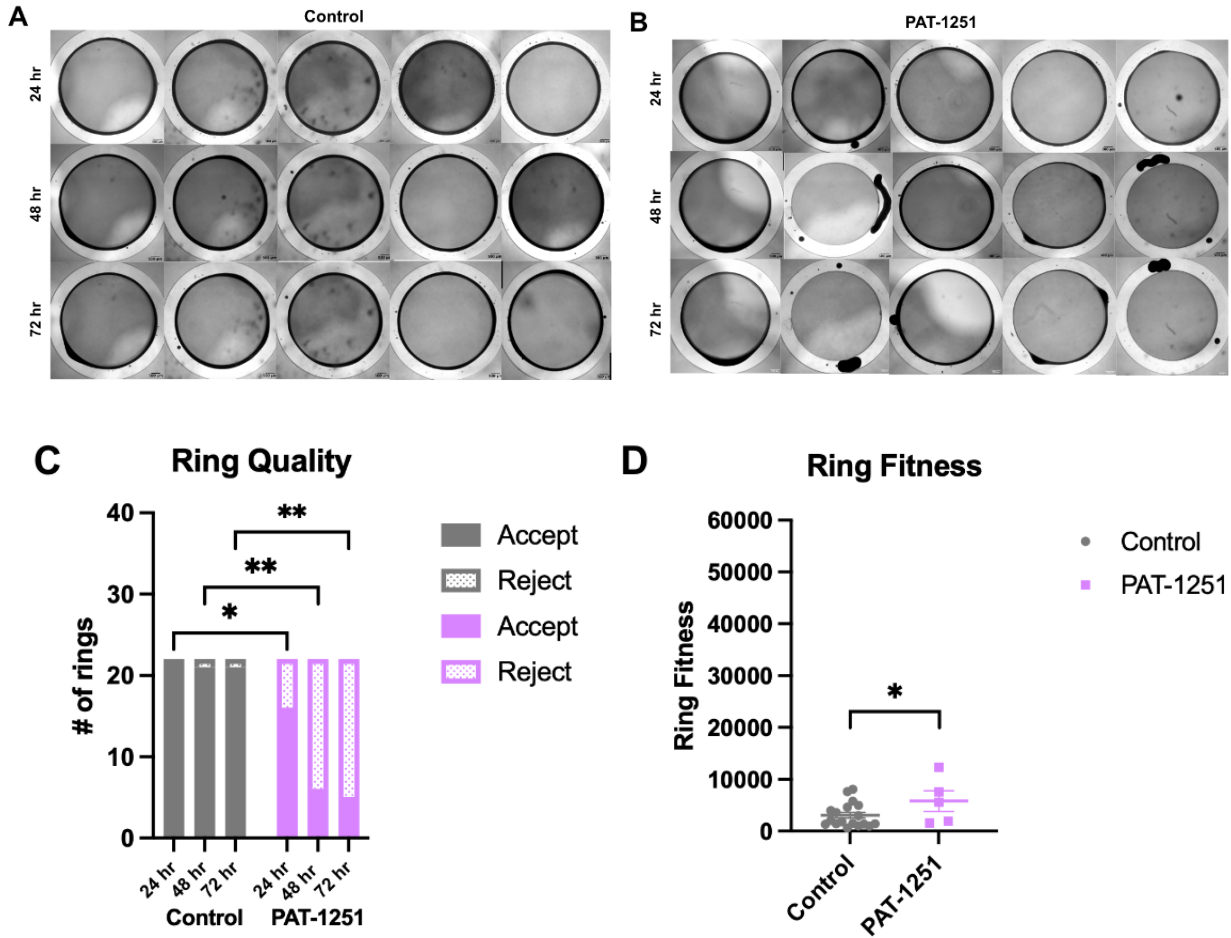


**Figure 10.** 3D tissue ring quality and fitness as a function of treatment. (A, B) Rings were treated with PAT-1251 at the time of cell-seeding and conventional view brightfield images acquired at 24, 48 and 72 hrs. after initial seeding. Brightfield images of the PAT-1251 and control rings were input into a custom Python code to analyze ring symmetry. Images were rejected from the program if no ring was detected, or inner and outer ring circles were not detected by the program. Scale bar=500  $\mu\text{m}$  for all images. (C) Ring quality was determined by the number of rings accepted or rejected by the software. Results were compared to control.  $n=22$  for both treatment groups. (D) Ring images at 72 hrs. that were accepted by the Python program were designated a fitness value  $\geq 0$ . A fitness value = 0 represents perfect ring symmetry while a fitness value  $>10,000$  is given to asymmetrical rings. Ring fitness is a unitless metric. Control  $n=21$ , PAT-1251  $n=5$ . The unique character \* denotes  $p<0.05$  and \*\* denotes  $p<0.01$  for both graphs.

## Ring Morphology Affects CSA and Volume of 3D Ring Tissues

PAT-1251 treatment of 3D ring tissues decreased tissue biomechanics. A change in ring morphology was also observed in ring tissues treated with PAT-1251 alone. As previously mentioned, ring thickness measurements in the  $x$ ,  $y$  and  $z$  dimensions are taken from equidistant, yet random locations along the tissues. If a change in ring morphology occurs, calculated CSA and volume measurements may also be altered if the non-uniformity of the ring tissues is not accurately accounted for. Since the aforementioned mechanical values were normalized to the CSA of each ring, any discrepancy in ring morphology could have greatly affected the calculated engineering UTS and MTM values.

Upon further investigation into the morphological changes induced in 3D ring tissues from PAT-1251 treatment, a large variance was found in  $x$ ,  $y$  ring thickness measurements. New thickness measurements from PAT-1251 rings were taken and divided into two categories: thin and thick segments. Rings were manually classified as either uniform or containing 1 or 2 “blebs” (**Figure 11A-C**). For the purpose of the experiment, blebs are defined as notable protrusions of ring tissue causing asymmetry. Rings containing these blebs were then classified as having just 1 or 2 such protrusions. For measuring the thick segments of a nonuniform ring tissue, rings only  $x$ ,  $y$  measurements from the thicker bleb were considered. The average thickness values from these categories were then compared to one another and to control (**Figure 11D**).

Average ring thickness of uniform PAT-1251 treated rings was significantly smaller than the average thickness of the large bleb seen in both 1 and 2 bleb rings ( $p < 0.005$  and  $p < 0.05$  respectively). With an average  $x$ ,  $y$  thickness of 118 micron, the thinnest portions of 2 bleb PAT-

1251 rings showed no significant difference in size compared to uniform control (158 micron) and uniform PAT-1251 (153 micron) rings. Aside from this similarity, large differences in thickness were observed between experimental groups and even within the same ring (thick vs thin segments). While the equidistant, random selection of points of measure for rings is meant to eliminate bias, it is masking the effect of ring morphology on ring thickness and indirectly on biomechanics.

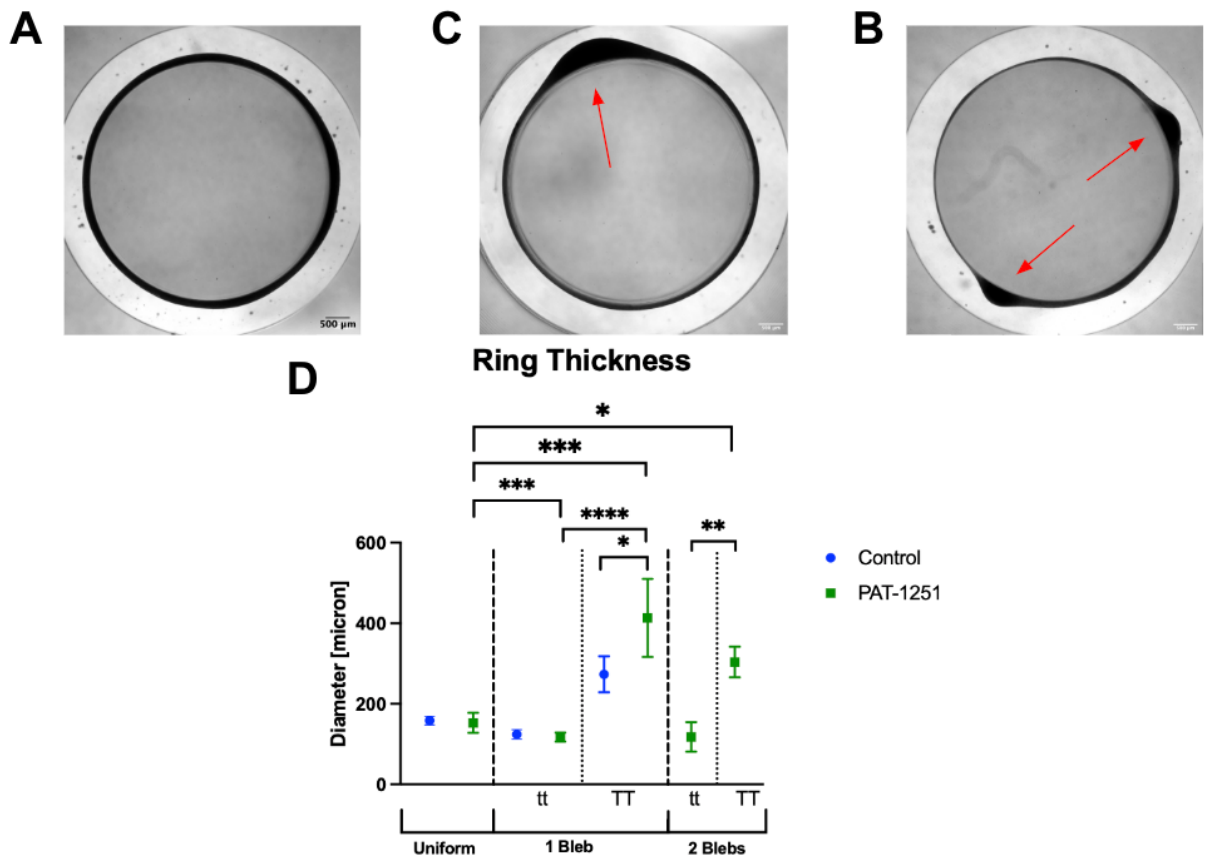


**Figure 11.** Average 3D ring tissue x, y thickness as a result of PAT-1251. (A-C) Conventional view brightfield images of PAT-1251 rings on day 14, representative of the 3 ring categories: uniform (A), 1 bleb (B), and 2 blebs (C). For all brightfield images, scale bar=500  $\mu\text{m}$ . Red arrows point to “blebs” or thick segments of the ring. (D) Ring thickness was measured in the x, y dimensions on ImageJ at 9 equidistant, random locations (uniform) or 9 equidistant, random locations of thin segments and an additional 6 equidistant, random locations of thick segments. Measurements were averaged and statistical analysis was performed between and intragroup using one sample t and Wilcoxon tests and ordinary one-way ANOVA with Tukey’s multiple comparisons test on GraphPad Prism 9.0. tt = thin thickness and TT = thick thickness. Control n=10 (uniform) and n=3 (1 bleb), and n=0 for 2 bleb measurements. PAT-1251 n=5 (uniform), n=8 (1 bleb), and n=3 (2 blebs). The unique character \* denotes  $p<0.05$ , \*\* denotes  $p<0.01$ , \*\*\* denotes  $p<0.0005$  and \*\*\*\* denotes  $p<0.0001$ .

## Discussion and Conclusions

The LOX family of enzymes are known key enzymes involved in the crosslinking of collagen in the ECM. This crosslinking increases collagen stability in the ECM while also increasing tissue biomechanics [4] LOX activity is positively correlated with fibrotic disease progression and overall ECM stiffness [6, 9, 10, 32]. Specifically, the enzyme LOXL2 is known to be synthesized by human dermal fibroblasts and its expression is positively correlated with ECM collagen levels [10, 33, 34]. Preventing collagen crosslinking by inhibiting LOX activity is of particular interest in the search of specific molecular targets in the development of new drug therapies in the treatment of fibrosis. PAT-1251 is a known inhibitor of LOX activity and its known specificity for LOXL2 makes it a desirable drug treatment for further study. In this experiment, we investigated PAT-1251's action on human dermal fibroblasts as the cells self-assemble into a 3D ring tissue over the course of 14 days *in vitro*. We found that biomechanics of PAT-1251 treated rings decreased compared to control.

TGF- $\beta$ 1 is an important growth factor synthesized by human fibroblasts and a key mediator of fibroblast activation and the pathogenesis of fibrosis [18, 19, 35]. A well known activity of TGF- $\beta$ 1 is its ability to stimulate fibroblasts to synthesize collagen and secrete collagen fibrils into the ECM [18, 35]. Previous studies have shown TGF- $\beta$ 1's ability to increase ring tissue CSA, volume and biomechanics in the same 3D fibroblast tissue model used in this experiment [29]. These results were reproduced in this study and compared to rings treated with TGF- $\beta$ 1 plus PAT-1251 to determine if the PAT-1251 drug treatment affects tissue biomechanics in a TGF- $\beta$ 1 stimulated environment. Introduction of TGF- $\beta$ 1 to the cellular environment activates the intracellular Smad2/Smad3 complex and JNK. Downstream of both of these pathways is increased transcription of LOX genes [2]. Therefore, rings treated with TGF- $\beta$ 1 plus

PAT-1251 in this study were likely experiencing increased LOX expression and irreversible inactivation of LOX in the ECM by PAT-1251. Our results suggest that PAT-1251 is able to decrease tissue strength and stiffness in a TGF- $\beta$ 1 stimulated environment despite no significant change in overall tissue size. The combination treatment of growth factor and drug suggest a sustained function of TGF- $\beta$ 1 mediated increase in tissue volume and simultaneous decrease in LOX mediated crosslinking of collagen fibrils, ultimately decreasing biomechanics. Additional studies measuring total collagen in PAT-1251 rings and rings treated with TGF- $\beta$ 1 plus PAT-1251 should be performed to validate this statement.

Utilizing ring thickness measurements from equidistant, random locations along the ring tissue, no significant difference in CSA or volume was observed between control and PAT-1251 groups, suggesting that PAT-1251 does not affect tissue morphology. However, brightfield images showed a significant change in ring morphology after drug treatment. Many rings appear asymmetrical, having 1 or 2 protrusions designated as “blebs.” When thickness measurements from these blebs were taken separate from measurements elsewhere on the ring, a significant difference was noted between the two groups suggesting PAT-1251 affects tissue morphology in addition to biomechanics.

Previous studies examining the effects of PAT-1251 on collagen crosslinking and fibrosis have found morphological changes in *in vitro* models indicating inhibition of LOX activity may contribute to abnormal morphology [36, 37]. Results from these studies reveal the contribution LOX enzymes, especially LOXL2, have on collagen fiber assembly and alignment. LOXL2 has been demonstrated to have a large effect on ECM morphology which influences cellular interactions and cell morphology [38]. The combination of these effects can lead to larger tissue morphological changes such as those seen with our 3D tissue rings treated with PAT-1251.

Further study of the morphological changes observed from PAT-1251 could be performed through histological analysis of fixed ring tissues on day 14. Staining with hematoxylin and eosin (H&E) and Mason's trichrome would showcase ECM composition and cell alignment. Multiphoton second-harmonic generation (SHG) imaging would similarly provide visualization of the ECM, especially collagen alignment and density [39]. Dose-response experiments using drug concentrations below or greater than the 10  $\mu$ M PAT-1251 used in this experiment would similarly provide better insight into the drug's effects. Performing imaging and tensile testing on ring tissues on days 7 and 21 would provide further clarity into the effects of PAT-1251 on ring morphology and biomechanics.

Further investigation into PAT-1251's mechanism of action is recommended to further understand its effect on fibrotic tissue. RT-qPCR for selected genes would better assess if differential gene expression might explain results from this study. Measuring expression of well-known markers for fibrotic phenotype ( $\alpha$ SMA, IL-6) and collagen subtypes (COL1A1, COL3A1, COL6A1) at day 14 would provide better assessment as to whether the drug and/or growth factor treatment had an effect on the ring tissues or if additional factors should be considered in explaining our data [32, 40, 41]. It would also be interesting to determine if TGF- $\beta$ 1 plus PAT-1251 alters the ratios of different collagen and LOX types at the protein level and if this correlates to change in biomechanics.

The results from this study highlight the benefits of using a 3D ring tissue model system to understand the different mechanisms involved in fibrosis and identifying molecular targets for new drug therapies. While this model lacks the biological complexity animal models provide, the ring system allows us to focus on one cell type. Most in vitro studies rely on 2D monolayer culturing of fibroblasts to measure drug and cytokine effects. Our 3D culturing of fibroblasts



produced a tissue that more closely models native tissue morphology and mechanical properties. We are able to culture our models for a substantially longer amount of time compared to 2D culture, allowing us to study drug and cytokine treatment effects in a time frame that more closely resembles the wound healing response *in vivo* [42].

## References

1. Wynn, T.A., *Cellular and molecular mechanisms of fibrosis*. J Pathol, 2008. **214**(2): p. 199-210.
2. Sethi, A., et al., *Transforming growth factor-beta induces extracellular matrix protein cross-linking lysyl oxidase (LOX) genes in human trabecular meshwork cells*. Invest Ophthalmol Vis Sci, 2011. **52**(8): p. 5240-50.
3. Adamiak, K. and A. Sionkowska, *Current methods of collagen cross-linking: Review*. Int J Biol Macromol, 2020. **161**: p. 550-560.
4. Lin, J., et al., *Mechanical Roles in Formation of Oriented Collagen Fibers*. Tissue Eng Part B Rev, 2020. **26**(2): p. 116-128.
5. Kumari, S., T.K. Panda, and T. Pradhan, *Lysyl Oxidase: Its Diversity in Health and Diseases*. Indian J Clin Biochem, 2017. **32**(2): p. 134-141.
6. Vallet, S.D. and S. Ricard-Blum, *Lysyl oxidases: from enzyme activity to extracellular matrix cross-links*. Essays Biochem, 2019. **63**(3): p. 349-364.
7. Ferreira, S., et al., *LOXL2 Inhibitors and Breast Cancer Progression*. Antioxidants (Basel), 2021. **10**(2).
8. Zhang, X., et al., *Crystal structure of human lysyl oxidase-like 2 (hLOXL2) in a precursor state*. Proc Natl Acad Sci U S A, 2018. **115**(15): p. 3828-3833.
9. Schilter, H., et al., *The lysyl oxidase like 2/3 enzymatic inhibitor, PXS-5153A, reduces crosslinks and ameliorates fibrosis*. J Cell Mol Med, 2019. **23**(3): p. 1759-1770.
10. Rowbottom, M.W., et al., *Identification of 4-(Aminomethyl)-6-(trifluoromethyl)-2-(phenoxy)pyridine Derivatives as Potent, Selective, and Orally Efficacious Inhibitors of*

- the Copper-Dependent Amine Oxidase, Lysyl Oxidase-Like 2 (LOXL2)*. J Med Chem, 2017. **60**(10): p. 4403-4423.
11. Janssen, R., *Lysyl Oxidase Inhibition by Heparin in Idiopathic Pulmonary Fibrosis: Is There Still Hope?* Am J Respir Crit Care Med, 2017. **195**(1): p. 141-142.
  12. Wang, H., et al., *A Novel In Situ Activity Assay for Lysyl Oxidases*. bioRxiv, 2021: p. 2021.04.30.442175.
  13. Findlay, A.D., et al., *Identification and Optimization of Mechanism-Based Fluoroallylamine Inhibitors of Lysyl Oxidase-like 2/3*. J Med Chem, 2019. **62**(21): p. 9874-9889.
  14. Gray, E., B. Mulloy, and T.W. Barrowcliffe, *Heparin and low-molecular-weight heparin*. Thromb Haemost, 2008. **99**(5): p. 807-18.
  15. Saito, T., T. Kotani, and K. Suzuki, *Antifibrotic therapy by sustained release of low molecular weight heparin from poly(lactic-co-glycolic acid) microparticles on bleomycin-induced pulmonary fibrosis in mice*. Sci Rep, 2020. **10**(1): p. 19019.
  16. Hinz, B., *The extracellular matrix and transforming growth factor-beta1: Tale of a strained relationship*. Matrix Biol, 2015. **47**: p. 54-65.
  17. Horiguchi, M., M. Ota, and D.B. Rifkin, *Matrix control of transforming growth factor-beta function*. J Biochem, 2012. **152**(4): p. 321-9.
  18. Borthwick, L.A., T.A. Wynn, and A.J. Fisher, *Cytokine mediated tissue fibrosis*. Biochim Biophys Acta, 2013. **1832**(7): p. 1049-60.
  19. Frangogiannis, N., *Transforming growth factor-beta in tissue fibrosis*. J Exp Med, 2020. **217**(3): p. e20190103.

20. *PAT-1251 in Treating Patients With Primary Myelofibrosis, Post-Polycythemia Vera Myelofibrosis, or Post-Essential Thrombocytosis Myelofibrosis.*  
<https://ClinicalTrials.gov/show/NCT04054245>.
21. Cosgrove, D., et al., *Lysyl oxidase like-2 contributes to renal fibrosis in Col4alpha3/Alport mice.* *Kidney Int*, 2018. **94**(2): p. 303-314.
22. *Single and Multiple Dose Safety, Tolerability, PK and Food Effect Study of PAT-1251 in Healthy Adult Subjects.* <https://ClinicalTrials.gov/show/NCT02852551>.
23. Lampi, M.C. and C.A. Reinhart-King, *Targeting extracellular matrix stiffness to attenuate disease: From molecular mechanisms to clinical trials.* *Science Translational Medicine*, 2018. **10**(422): p. eaao0475.
24. Wilks, B.T., et al., *Directing fibroblast self-assembly to fabricate highly-aligned, collagen-rich matrices.* *Acta Biomater*, 2018. **81**: p. 70-79.
25. Rhee, S., *Fibroblasts in three dimensional matrices: cell migration and matrix remodeling.* *Exp Mol Med*, 2009. **41**(12): p. 858-65.
26. Sensini, A. and L. Cristofolini, *Biofabrication of Electrospun Scaffolds for the Regeneration of Tendons and Ligaments.* *Materials (Basel)*, 2018. **11**(10).
27. Ristaniemi, A., et al., *Comparison of elastic, viscoelastic and failure tensile material properties of knee ligaments and patellar tendon.* *J Biomech*, 2018. **79**: p. 31-38.
28. Jin, Q., et al., *Mechanical Researches on Young's Modulus of SCS Nanostructures.* *Journal of Nanomaterials*, 2009. **2009**: p. 1-6.
29. Wilks, B.T., et al., *Quantifying Cell-Derived Changes in Collagen Synthesis, Alignment, and Mechanics in a 3D Connective Tissue Model.* *Adv Sci (Weinh)*, 2022. **9**(10): p. e2103939.

30. Adebayo, O., et al., *Self-assembled smooth muscle cell tissue rings exhibit greater tensile strength than cell-seeded fibrin or collagen gel rings*. J Biomed Mater Res A, 2013. **101**(2): p. 428-37.
31. Gwyther, T.A., et al., *Engineered vascular tissue fabricated from aggregated smooth muscle cells*. Cells Tissues Organs, 2011. **194**(1): p. 13-24.
32. Nguyen, X.X., et al., *Lysyl oxidase directly contributes to extracellular matrix production and fibrosis in systemic sclerosis*. Am J Physiol Lung Cell Mol Physiol, 2021. **320**(1): p. L29-L40.
33. Barry-Hamilton, V., et al., *Allosteric inhibition of lysyl oxidase-like-2 impedes the development of a pathologic microenvironment*. Nat Med, 2010. **16**(9): p. 1009-17.
34. Ikenaga, N., et al., *Selective targeting of lysyl oxidase-like 2 (LOXL2) suppresses hepatic fibrosis progression and accelerates its reversal*. Gut, 2017. **66**(9): p. 1697-1708.
35. Kendall, R.T. and C.A. Feghali-Bostwick, *Fibroblasts in fibrosis: novel roles and mediators*. Front Pharmacol, 2014. **5**: p. 123.
36. Grossman, M., et al., *Tumor Cell Invasion Can Be Blocked by Modulators of Collagen Fibril Alignment That Control Assembly of the Extracellular Matrix*. Cancer Res, 2016. **76**(14): p. 4249-58.
37. Shifren, A. and R.P. Mecham, *The stumbling block in lung repair of emphysema: elastic fiber assembly*. Proc Am Thorac Soc, 2006. **3**(5): p. 428-33.
38. Wong, K.S., et al., *Self-supervised classification of subcellular morphometric phenotypes reveals extracellular matrix-specific morphological responses*. Sci Rep, 2022. **12**(1): p. 15329.

39. Hopkins, C.M.W.B.T.M., J. R. , *TGF- $\beta$ 1 requires IL-13 to sustain collagen accumulation and increasing tissue strength and stiffness*. 2022, Brown University.
40. Muhl, L., et al., *Single-cell analysis uncovers fibroblast heterogeneity and criteria for fibroblast and mural cell identification and discrimination*. Nat Commun, 2020. **11**(1): p. 3953.
41. Shinde, A.V., C. Humeres, and N.G. Frangogiannis, *The role of alpha-smooth muscle actin in fibroblast-mediated matrix contraction and remodeling*. Biochim Biophys Acta Mol Basis Dis, 2017. **1863**(1): p. 298-309.
42. Gurtner, G.C., et al., *Wound repair and regeneration*. Nature, 2008. **453**(7193): p. 314-21.